POLYPUBLIE

Intraoperative use of high-speed Raman spectroscopy during soft tissue sarcoma resection

Jean-Philippe Dulude, Alice Le Moël, Frédérick Dallaire, Josée Doyon, Kirk Urmey, Eric Marple, Guy Leblanc, Georges Basile, Sophie Mottard, Marc Isler, Frédéric Leblond, Mai-Kim Gervais

Document en libre accès dans PolyPublie
Open Access document in PolyPublie

Date	2025
Type	Article de revue / Article
Version	Version officielle de l'éditeur / Published version
URL de PolyPublie **PolyPublie URL**	https://publications.polymtl.ca/63362/
Évaluation par les pairs **Peer reviewed**	Révisé par les pairs / Refereed
Conditions d'utilisation **Terms of use**	Creative Commons Attribution-Utilisation non commerciale-Pas d'oeuvre dérivée 4.0 International / Creative Commons Attribution-NonCommercial-NoDerivatives 4.0 International (CC BY-NC-ND)
Référence **Citation**	Dulude, J.-P., Le Moël, A., Dallaire, F., Doyon, J., Urmey, K., Marple, E., Leblanc, G., Basile, G., Mottard, S., Isler, M., Leblond, F., & Gervais, M.-K. (2025). Intraoperative use of high-speed Raman spectroscopy during soft tissue sarcoma resection. Scientific Reports, 15, 8789 (13 pages). https://doi.org/10.1038/s41598-025-93089-z

Publication officielle
Official publication

Titre de la revue **Journal title**	Scientific Reports (vol. 15)
Maison d'édition **Publisher**	Nature
URL officielle **Official URL**	https://doi.org/10.1038/s41598-025-93089-z
Mention légale **Legal notice**	This article is licensed under a Creative Commons Attribution-NonCommercial-NoDerivatives 4.0 International License, which permits any non-commercial use, sharing, distribution and reproduction in any medium or format, as long as you give appropriate credit to the original author(s) and the source, provide a link to the Creative Commons licence, and indicate if you modified the licensed material. You do not have permission under this licence to share adapted material derived from this article or parts of it. The images or other third party material in this article are included in the article's Creative Commons licence, unless indicated otherwise in a credit line to the material. If material is not included in the article's Creative Commons licence and your intended use is not permitted by statutory regulation or exceeds the permitted use, you will need to obtain permission directly from the copyright holder. To view a copy of this licence, visit http://creativecommons.org/licenses/by-nc-nd/4.0/.

Ce fichier a été téléchargé à partir de PolyPublie, le dépôt institutionnel de Polytechnique Montréal
This file has been downloaded from PolyPublie, the institutional repository of Polytechnique Montréal
https://publications.polymtl.ca

scientific reports

Check for updates

OPEN

Intraoperative use of high-speed Raman spectroscopy during soft tissue sarcoma resection

Jean-Philippe Dulude[1,2], Alice Le Moël[1,3], Frédérick Dallaire[1,3], Josée Doyon[2,4], Kirk Urmey[5], Eric Marple[5], Guy Leblanc[2,4], Georges Basile[2,4], Sophie Mottard[2,4], Marc Isler[2,4], Frederic Leblond[1,3]✉ & Mai-Kim Gervais[2,4]✉

Retroperitoneal soft tissue sarcoma (RSTS) is a rare type of cancer with limited treatment options. Achieving complete resection with negative margins is one of the most significant prognostic factors for RSTS survival. The UltraProbe is a handheld point probe Raman spectroscopy system that significantly decreases the imaging time compared to the probe systems currently used. This study aims to determine the performance of the UltraProbe in detecting STS in an in vivo environment during their resection. Thirty patients were recruited at Maisonneuve-Rosemont Hospital, Montreal, Canada. Raman spectra were acquired during STS resection using the instrument. A machine learning random forest classification algorithm was developed to predict the diagnosis associated with new Raman spectra: STS or healthy tissue. The classification of Raman spectra as well-differentiated liposarcomas or normal adipose tissue was performed with a sensitivity of 94%, specificity of 95%, and accuracy of 94%. The classification of spectra as well-differentiated and dedifferentiated liposarcomas or normal adipose tissue was performed with a sensitivity of 90%, specificity of 93%, and accuracy of 90%. The classification of spectra as non-liposarcoma STS or protein-rich non-adipose tissue was performed with a sensitivity of 87%, specificity of 81%, and accuracy of 87%.

Soft tissue sarcomas (STS) are a rare type of cancer arising from mesenchymal cells. They represent a vast and heterogenous pathological entity, with over 100 histological subtypes per the 2020 World Health Organization Soft Tissue and Bone Tumours Classification[1]. Prognosis and management are highly dependent on histological subtype and location. Retroperitoneal soft tissue sarcomas (RSTS) form a subclass of STS arising in the retroperitoneum, an anatomical space located in the posterior portion of the abdominal cavity. RSTS have an incidence rate of approximately 2.7 cases per million-population[2]. The most common subtypes of RSTS are dedifferentiated liposarcoma (DDLPS), well-differentiated liposarcomas (WDLPS), and leiomyosarcoma (LMS)[3].

RSTS can be challenging to diagnose and to treat. Individual RSTS management depends on tumor biology, location, grade, histologic subtype and tumor size. Completeness of resection is a key element for improved survival. Due to the rarity of the disease, they should be managed in high-volume cancer centers dedicated to sarcoma. The multi-disciplinary team involved in sarcoma treatment includes surgical oncologists, medical oncologists, radiation oncologists, pathologists, and radiologists, all possessing a specific expertise in STS. It has been demonstrated that patients treated in high-volume centers had a higher rate of complete resection and an improved survival[4].

Surgical resection represents the cornerstone of RSTS treatment. The margin status is a major prognostic factor. It is also one of the only modifiable prognostic factors. It has been clearly demonstrated that surgery with macroscopically positive (R2) resection margins produces significantly worse outcome when compared to microscopically positive (R1) margins or microscopically negative (R0) margins[5–9]. However, the literature is not as clear regarding the outcome superiority of R0 versus R1 resections, although there appears to be a trend favoring R0 resection for both overall survival and recurrence-free survival[10–14].

To perfor a complete resection, the favored surgical approach is aggressive retroperitoneal compartment resection. This surgical strategy is defined as *en bloc* resection of any organ within 1–2 centimeters of the tumor, with the goal of increasing rates of complete tumor resection. This can result in ipsilateral nephrectomy, hemicolectomy, psoas fascia resection, vascular resection, other viscera resection and complete removal of all

[1]Polytechnique Montréal, Montreal, Canada. [2]Université de Montréal, Montreal, Canada. [3]Centre de recherche du Centre Hospitalier de l'Université de Montréal, Montreal, Canada. [4]Hôpital Maisonneuve-Rosemont, Montreal, Canada. [5]EmVision LLC, Loxahatchee, FL, USA. ✉email: frederic.leblond@polymtl.ca; mai-kim.gervais.med@ssss.gouv.qc.ca

adipose tissue in the ipsilateral retroperitoneum. Bonvalot et al. demonstrated that aggressive multivisceral resection resulted in better local control, with significantly reduced intra-abdominal recurrences at 5 years[11]. Gronchi et al. further demonstrated an improvement in overall survival following compartmental resection[15]. As expected, higher morbidity resulted from this aggressive surgical approach[16].

Neoadjuvant or adjuvant radiotherapy is an adjunct treatment to surgery and is used in specific cases. The STRASS-1 trial is a randomized controlled multicentric trial comparing the use of preoperative radiotherapy followed by RSTS resection surgery versus RSTS resection only[17]. Those results published in 2020 indicate neoadjuvant radiotherapy did not improve abdominal recurrence-free survival. Post-hoc subgroup sensitivity analysis for patients with WDLPS and low-grade sarcomas showed that there was a small increase of abdominal recurrence-free survival in the radiotherapy group. Hence, radiotherapy is not used routinely as a neoadjuvant treatment option for RSTS but can be considered in select cases.

Adjuvant chemotherapy has not shown survival benefit for RSTS. Retrospective trials have given contradicting evidence[18–22], and some prospective trials have failed to show an increase in overall or recurrence free survival[23]. The ongoing STRASS-2 trial might provide a more definitive answer regarding the benefit of neoadjuvant chemotherapy. This phase III trial studies the use of pre-operative doxorubicin with ifosfamide for high-grade liposarcoma and doxorubicin with dacarbazine for LMS.

As completeness of resection represents one of the main prognostic factors to optimize survival outcomes, new technologies are needed to achieve this surgical goal. Raman spectroscopy is an optical analysis technique based on the detection and quantification of inelastically scattered light. Raman scattering occurs following interaction between photons and material samples[24]. Although most of the scattering occurs as elastic Rayleigh scattering, a small proportion of scattering interactions are inelastic. In such cases, an energy exchange occurs between the sample and the incident photon. The result is a scattered photon with a shifted wavelength compared to the incident photon[25]. The intensity and wavelength of the Raman photons are dependent on the sample's molecular bonds and vibrational modes[26]. The most common type of scattering is Raman Stokes scattering, where the sample absorbs a small amount of the incident photon's energy as vibrational energy. Since photon energy is proportional to frequency, and inversely proportional to wavelength, scattered photons have a shorter wavelength. Rarely, if the sample is at a higher vibrational energy level than its ground state, the scattering molecule loses vibrational energy during the interaction, and the scattered photon has a longer wavelength. This is known as anti-Stokes Raman scattering. Given the natural distribution heavily favouring ground state excitation levels at room temperature, Stokes Raman scattering is more prevalent by several orders of magnitude[27].

Detection of Raman scattering following sample illumination with a fixed wavelength laser source creates a spectrum of intensity of scattered photons based on Raman shift. Different types of biological tissues exhibit varying proportions of basic molecular compounds, each made of arrays of specific vibrational molecular bonds[28,29]. Each type of tissue has a distinctive Raman spectrum which can be used in its identification. The peaks making up the Raman spectra can often be explained by the presence of specific compounds. Adipose tissue contains high concentrations of various lipids, such as fatty acids, triacyglycerol, cholesterol, and membrane lipids[30]. These lipids have distinct Raman spectra, but present common characteristics. These include a peak seen at 1440 cm^{-1} caused by the presence of CH_2 and CH_3 bonds scissoring, at 1670 cm^{-1} caused by stretching of the C = C bond, at 1300 cm^{-1} caused by twisting of the CH_2 bond, and at 1420 cm^{-1} caused by the bending of the CH_2 bond[31]. These bonds are present in great amounts in lipids, which are present in significant amounts in adipose cells[32]. The superposition of these peaks creates a unique spectrum, which can act as the sample's signature. Significant change in the tissue's composition, as is the case following neoplastic transformation, results in significant change in the tissue's Raman spectrum. Mutations responsible for neoplastic transformation alter the cell's proteinic expression, in addition to modifications in the nucleic acid[33] and membrane phospholipids compositions[34]. Together, these biomolecular changes have an impact on a sample's overall molecular makeup and can result in a modification of the sample's Raman spectrum. These modifications can in turn be used to detect the presence of cancer in a tissue sample. Raman spectroscopy has shown promising results in the detection of multiple cancer types, including breast[35–37], brain[38–40], gastric[41], colon[42], and melanoma[43].

A significant hurdle to the clinical integration of Raman-based instruments is the prohibitively large Raman photon collection times. Both hardware and tissue characteristics influence imaging times. Tissue absorption and elastic scattering modulate the overall photonic signal-to-noise ratio (SNR) associated with fluorescence and inelastically scattered photons. SNR is calculated as the square root of the total photon count at a single point. The ratio of intrinsic fluorescence to Raman scattering ratio, or signal-to-background ratio (SBR), directly impacts the ability of a system to detect a tissue Raman signature with high sensitivity. Signal-to-background ratio can vary dramatically depending on which tissue type is interrogated, with most applications requiring large dynamical range sensors to ensure sufficiently large number of Raman photons can be captured over backgrounds that can be orders of magnitude larger. Background sources are typically not limited to intrinsic tissue fluorescence. They can also include instrument response contributions such as light source filters bleed-through, fluorescence from optical fibers, and interference filters. As a result of these considerations, the performance of a Raman system should be evaluated by its ability to acquire inelastically scattered light rapidly using high dynamical range sensors, and with low instrument-generated backgrounds.

This work presents the development of the UltraProbe, a new system that reduces integration time, and compares its performance with the previous generation of Raman spectroscopy probe used by our group to demonstrate ex vivo cancer detection in brain[44–46], breast[47], prostate[48,49], lung[50], and ovarian tissue[51]. Results of its use are presented in an in vivo setting during the surgical resection of STS. The acquired Raman spectra were used to develop and train a machine learning random forest classification algorithm to accurately predict Raman spectra diagnosis: healthy tissue or STS.

Results

Next generation hand-held Raman spectroscopy probe systems

A new Raman probe system (Class 2) was designed and developed –herein referred to as the UltraProbe– with the objective to reduce the imaging time required while keeping the same levels of SNR and SBR. The new system had several characteristics that differed from the previous device (Class 1) that led to improved light collection efficiency, both at the probe (Fig. 1b) and at the spectrometer (Fig. 1a) design levels (Methods). These characteristics include a probe design with 21 multi-mode detection fibers rather than seven, a spectrometer with a larger collection lens, and a slit having a larger aperture area designed to maximize light throughput while keeping the same spectral resolution as the Class 1 devices. The new UltraProbe system was equipped with data acquisition software optimizing signal quality through automated adjustment of the sensor exposure time for each measurement[52]. The SNR was optimized by maximizing usage of the dynamical range of the CCD sensor for light collection. This was done ensuring laser light exposure was always below the maximal permissible exposure (MPE) for skin as set by the ANSI laser safety standards[53] (Methods).

Tissue phantom experiments were conducted to compare the performance of the Class 1 and Class 2 devices at fixed exposure times. To compare both systems, olive oil was selected as an organic material because of its easily identifiable Raman peaks and high fluorescence background. An aluminum substrate was used as a container because of its low background compared to standard substrates such as glass slides[54]. An aluminum vial was filled with 1 cm of store-bought olive oil. The probes from Class 1 and Class 2 instruments were sequentially positioned near the olive oil surface, and measurements made at the surface with a fixed laser power set at $I = 50$ mW. Different exposure times per measurement (T) were done, with 10 milliseconds increments until saturation, with 25 repetitions (N). Standard data processing steps of cosmic ray removal and x- and y-axis calibration were applied to each individual measurement. The resulting Raman spectra were averaged over the N repeat measurements. The standard deviation for each spectral bin was computed (Methods). This resulted in spectra covering the spectral domain from 400 to 2000 cm^{-1} with a spectral resolution of approximately 5 mm^{-1}.

The spectra acquired with both Class 1 and Class 2 devices were plotted for $T = 50$, 100 and 150 ms (Fig. 2). Overall, the Class 2 probe acquired signal with an intensity increased by more than one order of magnitude when compared to the Class 1 probe, for the same illumination power and exposure times. The overall photon count associated with the Raman signal acquired with both probes was plotted as a function of exposure time with the y-axis (photonic count) on a logarithmic scale (Fig. 2). The photon count signal that was plotted corresponds to the Raman signal detected after background removal with the BubbleFill algorithm (Methods). This confirmed that the inelastically scattered signal after fluorescence background removal was more than 10 times larger for the Class 2 probe when compared to the Raman signal acquired with the Class 1 probe. Representative spectra acquired with both probes were then plotted, with one spectrum for the Class 1 probe acquired with $T = 1000$ ms, and one spectrum for the Class 2 probe acquired with $T = 150$ ms. The SNR was computed for the lipid bands centered at 824 cm^{-1} and 1440 cm^{-1}. For the band centered at 824 cm^{-1}, the obtained SNR was 110 for the Class 1 probe, and 118 for the Class 2 probe. For the 1440 cm^{-1} band, the SNR was 540 for the Class 1 probe and 584 for the Class 2 probe (Fig. 3). These results, computed for two representative spectra, demonstrate the

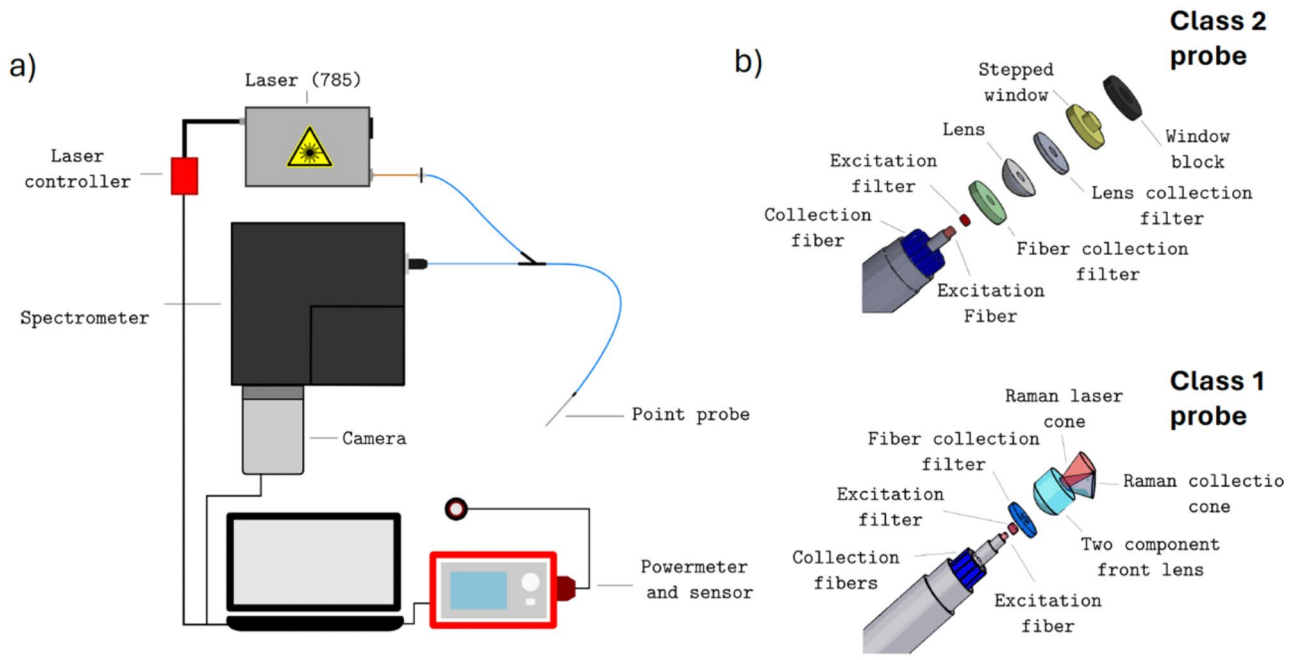


Fig. 1. Class 2 Raman point probe system schematization illustrating the basic components (**a**), and a comparison of the main point probe distinguishing features between class 1 and class 2 systems (**b**).

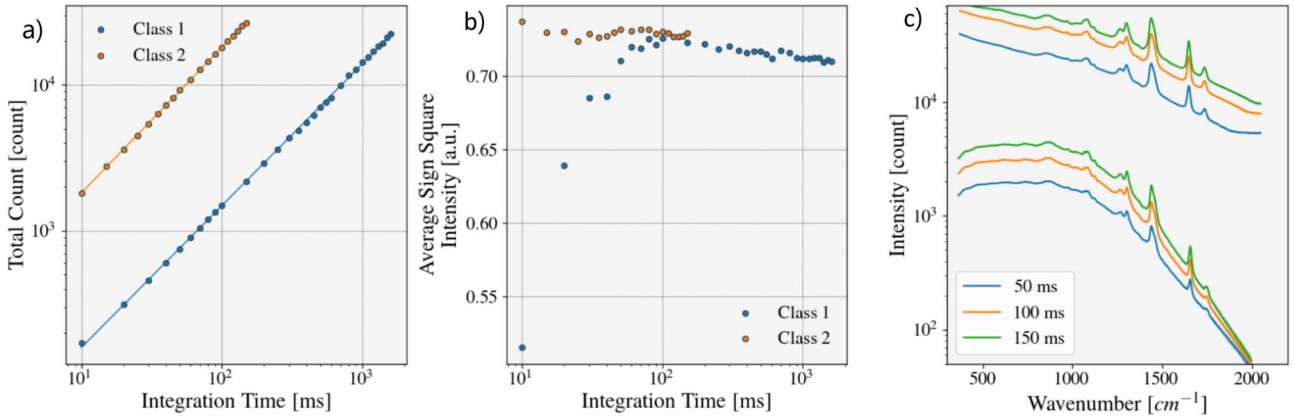


Fig. 2. Performance comparison between class 1 and class 2 Raman spectroscopy point probe systems regarding total photon count as a function of integration time (**a**), average sign square intensity as a function of integration time (**b**), and olive oil spectra acquired with varying exposure times of 50, 100, and 150 ms (**c**).

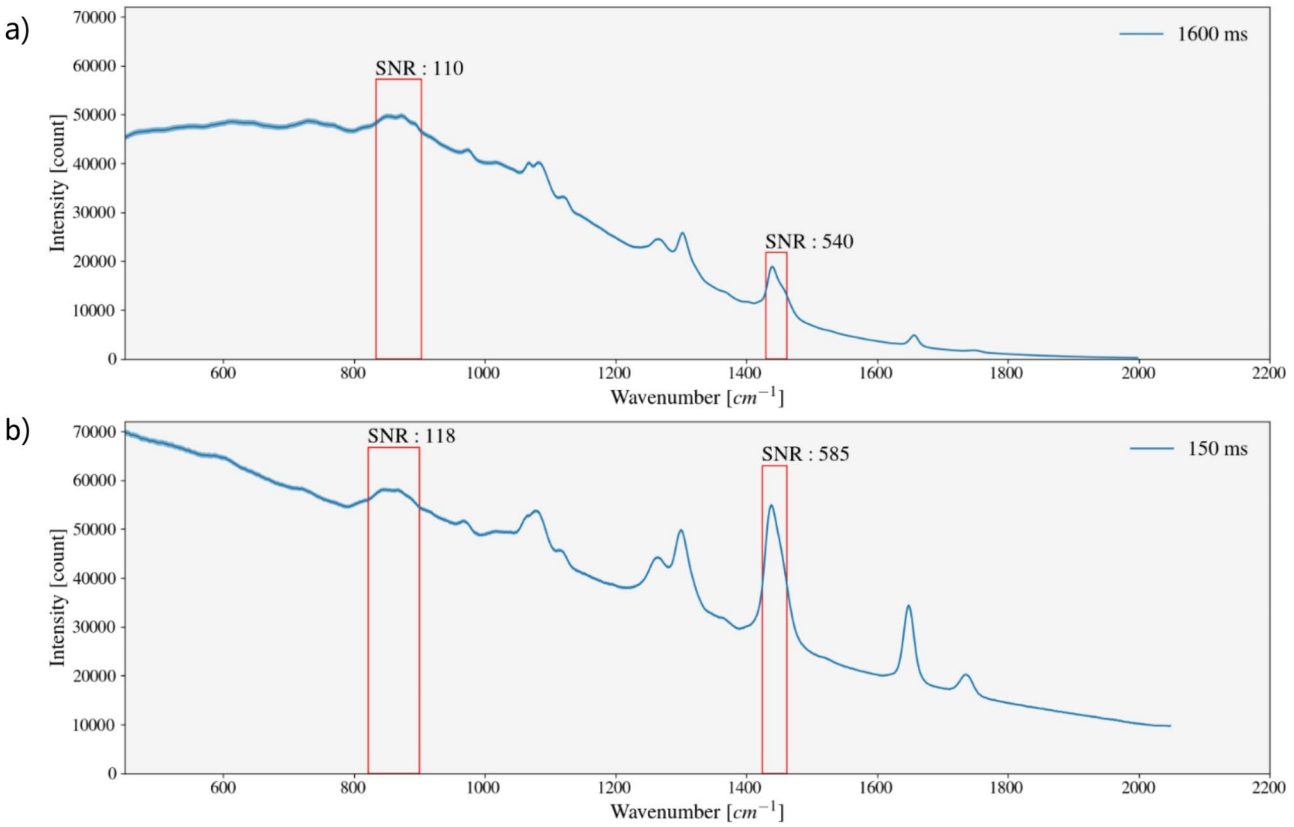


Fig. 3. Comparison of representative olive oil Raman spectra acquired using an exposure time of 1000 ms with a class 1 system (**a**), and an exposure time of 150 ms with a class 2 system (**b**).

equivalency of the measured signal quality between the probes, albeit with reduced integration times by a factor more than 10 for the Class 2 probe.

In the context of in vivo and ex vivo Raman spectra acquisition made during STS resection, the mean acquisition time for a single spectrum was 276 ms, ranging from 16 to 550 ms. On average, 25 Raman spectra were generated and averaged to create a single acquisition, which is a greater number than necessary. This was done to ensure the highest possible quality of spectra was used to train a machine learning classification algorithm and obtain the most accurate predictions.

Patient recruitment and pathology

Thirty patients with STS were recruited at Maisonneuve-Rosemont Hospital in Montreal, Canada between January 2022, and June 2023 (Table 1). Twenty-four patients had RSTS while 6 patients had an extremity STS. All but two patients underwent resection surgery with curative intent. Median age was 57.5 years old, with equal distribution between males and females. After evaluation by a sarcoma expert pathologist from our institution, final histopathological diagnosis was liposarcoma for 15 participants (50%). Of these, 10 (33.3%) were well-differentiated liposarcomas (WDLPS), and five (16.7%) were dedifferentiated liposarcomas (DDLPS). Five (16.7%) patients had leiomyosarcoma (LMS), three (10%) had undifferentiated pleomorphic sarcoma (UPS), one (3.3%) had a solitary fibrous tumor (SFT), and one (3.3%) had a myxofibrosarcoma (MFS). For five (16.7%) patients, final histopathology revealed an absence of malignant tissue, and the final diagnoses were retroperitoneal lipomas.

Data consistency between ex vivo and in vivo datasets

In vivo study of neoplastic tissue in humans has multiple inherent limitations. Most of these derive from the fundamental principle that the patient's optimal oncologic outcome cannot be compromised by the experiment. During oncologic surgery, tumors are often resected with a margin of healthy tissue surrounding the specimen to ensure a resection margin free of cancer cells. As a result, neoplastic tissue is often not actually visible or accessible during the procedure. Cutting through the tumor would violate the tumor's capsule, and potentially cause seeding of cancerous cells within the surgical field. This would significantly compromise the patient's outcome. As a result, analysis of in vivo tumoral properties with an optical device is particularly challenging.

To evaluate STS tissue samples using Raman spectroscopy without compromising margin resection status or risking intraoperative tumor dissemination, all cancer measurements were acquired ex vivo shortly after *en bloc* resection of the specimen. STS spectra were thus acquired in an ex vivo setting. However, an experimental protocol was implemented to study potential changes in the Raman signature of tissue that could be solely due

Number of participants	30
Age (median)	57.5
Sex	
Male	15 (50%)
Female	15 (50%)
Diagnosis	
Liposarcoma	15 (50%)
WDLPS	10 (33.3%)
DDLPS	5 (16.7%)
Leiomyosarcoma	5 (16.7%)
Undifferentiated pleomorphic sarcoma	3 (10%)
Myxofibrosarcoma	1 (3.3%)
Solitary fibrous tumor	1 (3.3%)
Lipoma	5 (16.7%)
Tumor grade	
Grade 1	1 (3.3%)
Grade 2	5 (16.7%)
Grade 3	10 (33.3%)
N/A	14 (46.7%)
Median tumor size (cm)	13
Resection margin status	
R0	21 (70%)
R1	7 (23.3%)
R2	2 (6.7%)
Multi-organ resection	
Yes	19 (63.3%)
No	11 (36.7%)
Recurrent disease	
Yes	4 (13.3%)
No	26 (86.7%)
Neoadjuvant radiotherapy	
Yes	5 (16.7%)
No	25 (83.3%)
Median ASA score	2

Table 1. Clinicopathologic features of participant population.

to the change in measurement conditions, i.e. *ex vivo versus in vivo* measurements (Methods). The changes in Raman spectra of biological tissue following resection were assessed to ensure spectra acquired in vivo and spectra acquired on freshly resected ex vivo tissue could be used to train the cancer detection machine learning models without introducing biases. During the resection surgery of five participants, spectra were acquired from samples of adipose, muscle, and fibrous tissue at multiple time points between 0 min (in vivo) and 90-minutes (ex vivo) following sample resection. No significant changes were detected when the Raman spectra were acquired within 60 min of sample resection. The average Raman spectra of adipose tissue at these time points were plotted to show the absence of time-dependent signal variation within the timeframe of the study. The intensity of significant peaks of lipid Raman spectra at these time points were also represented in a box plot to further illustrate the similarity in signal from the in vivo and ex vivo samples (Supplementary Fig. 1).

Intraoperative data acquisition and histopathology

The UltraProbe Raman spectroscopy system was used to acquire in situ spectroscopic data during STS resection surgery from normal tissue structures distant from the tumor site. Spectra were acquired in vivo from normal adipose, muscle, and fibrous tissue. Raman spectra were also acquired from these macroscopically identified tissue types at the resection margins following complete STS resection. This resulted in a normal tissue dataset made of 412 adipose tissue spectra, 155 muscle spectra, and 100 fibrous tissue spectra (Table 2).

The spectral dataset associated with tumor tissue was acquired ex vivo following tumor resection. STS specimens were taken to the pathology laboratory for Raman spectroscopy measurements after inking, slicing, and macroscopic evaluation by the pathologist. Spectroscopic data was acquired from the central portion of the specimens, distant from the inked margins to ensure the ink did not interfere with the biological tissue signal. A tissue sample of approximately 10 mm was then excised at the location of the acquisition and subsequently examined by an expert pathologist to provide a histopathological diagnosis linked to each Raman measurement. This resulted in 187 spectra associated with well-differentiated liposarcoma (WDLPS), 70 spectra associated with dedifferentiated liposarcoma (DDLPS), 59 spectra associated with leiomyosarcoma, 30 spectra associated with undifferentiated pleomorphic sarcoma, 20 spectra associated with myxofibrosarcoma and 18 spectra associated with solitary fibrous tumor. Sixty-two spectra associated with necrotic tissue were also acquired within sarcoma specimens and categorized as protein-rich, non-neoplastic tissue, for a total of 1,113 spectra (Table 2).

Data quality segregation prior to machine learning modeling

A quality factor (QF) metric was computed for each spectrum that allowed to evaluate their spectral quality (Methods). QF was used to automatically dismiss poor quality spectra with high levels of stochastic noise. Only spectra with QF ≥ 0.6 were used for classification training, representing 998 spectra (Table 2). The average Raman spectra of different histologic tissue subtypes, for both healthy tissue and STS were plotted along with the standard deviation associated with each spectral bin (Fig. 4).

Cancer detection machine learning models

Machine learning classification models were trained to predict the histopathologic diagnostic category of each tissue sample from which a Raman spectrum was acquired. The Raman spectra acquired were split into distinct datasets to perform classification based on biological and microscopic tissue similarity, thus providing clinically relevant tissue analysis. The first group (*adipose-rich*) contained the spectra of healthy adipose tissue and liposarcomas: WDLPS and DDLPS. A sub-group contained Raman spectra from healthy adipose tissue and WDLPS only. WDLPS is the most common subtype of liposarcomas, and its macroscopic appearance is very similar to that of healthy adipose fat, posing the greatest challenge in intraoperative resection margin assessment.

Tissue types	Number of Raman spectra	Number of Raman spectra after QF cut-off applied
Adipose-rich tissue	669	629
Liposarcoma	257	255
WDLPS	187	186
DDLPS	70	69
Healthy adipose tissue	412	374
Protein-rich tissue	444	369
Leiomyosarcoma	59	58
Undifferentiated pleomorphic sarcoma	30	26
Myxofibrosarcoma	20	20
Solitary fibrous tumor	18	18
Muscle	155	99
Fibrosis	100	92
Necrosis	62	56
Total	1113	998

Table 2. Number of spectra per tissue category both before and after applying a 0.6 QF cutoff.

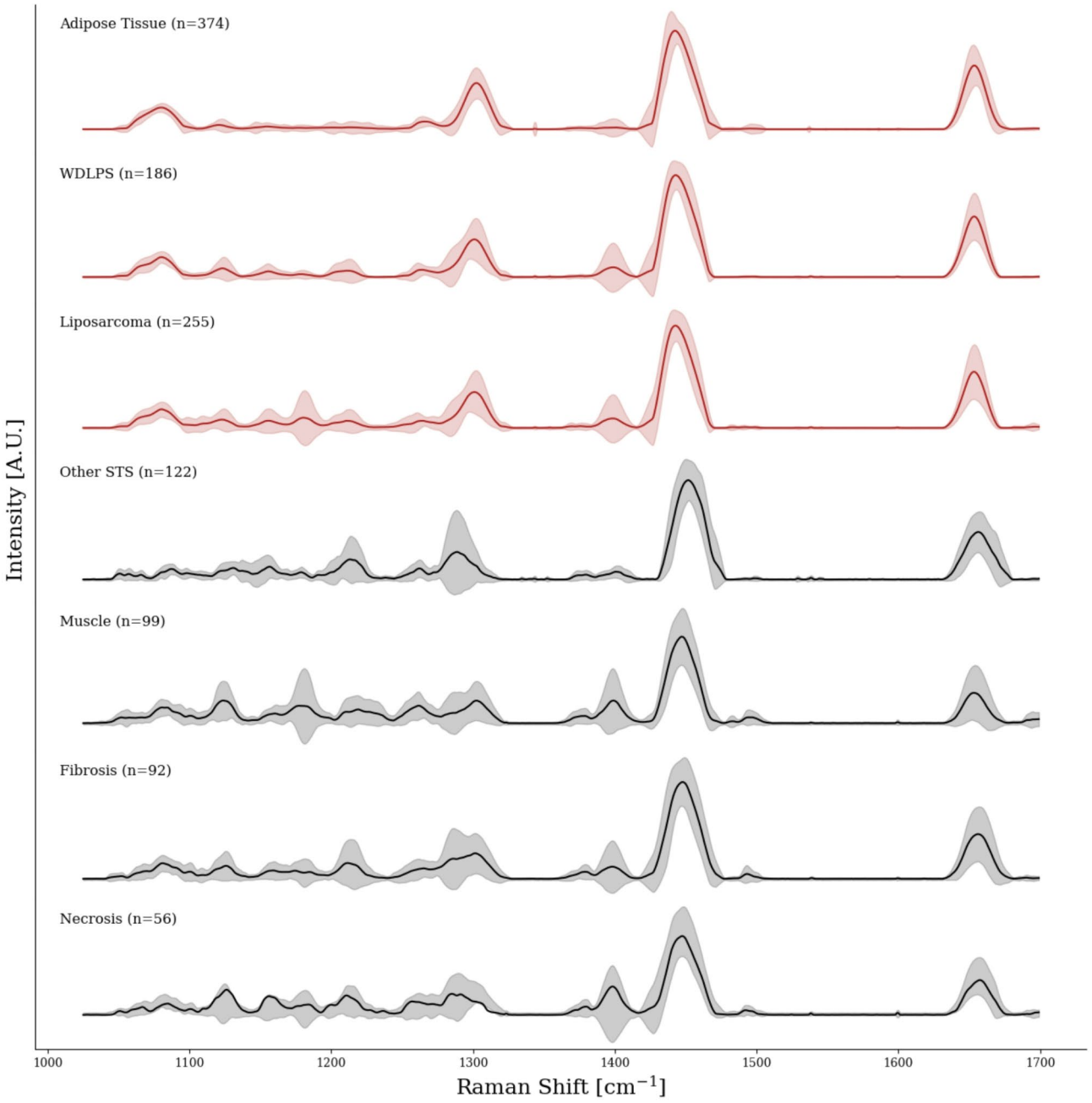


Fig. 4. Average Raman spectra with shaded standard deviation of the different tissue samples used in the random forest classification algorithms.

Both WDLPS and healthy adipose fat are easily distinguishable macroscopically from other types of normal tissue. The third group (*protein-rich*) contained spectra from all non-liposarcoma STS (LMS, UPS, SFT, MFS) and non-adipose non-sarcoma tissue, namely muscle, fibrotic tissue, and necrotic tissue.

Using these groups, three classification algorithms were developed to identify spectra in clinically relevant scenarios (Methods). Receiver-operating characteristic (ROC) curve analyses were performed to evaluate the performance of each model (Fig. 5). Classification of liposarcomas versus healthy adipose tissue resulted in a sensitivity of 90%, a specificity of 93%, and an accuracy of 90%. Classification of WDLPS versus healthy adipose tissue resulted in a sensitivity of 94%, a specificity of 95%, and an accuracy of 94%. Classification of non-liposarcoma STS versus non-adipose healthy tissue resulted in a sensitivity of 87%, an accuracy of 81%, and accuracy of 87%.

Discussion

The presented results show that Raman spectroscopy can be used as a technique to detect STS in an in vivo setting. Its sensitivity, specificity and accuracy were greater than 80% across all types of sarcomas, and greater

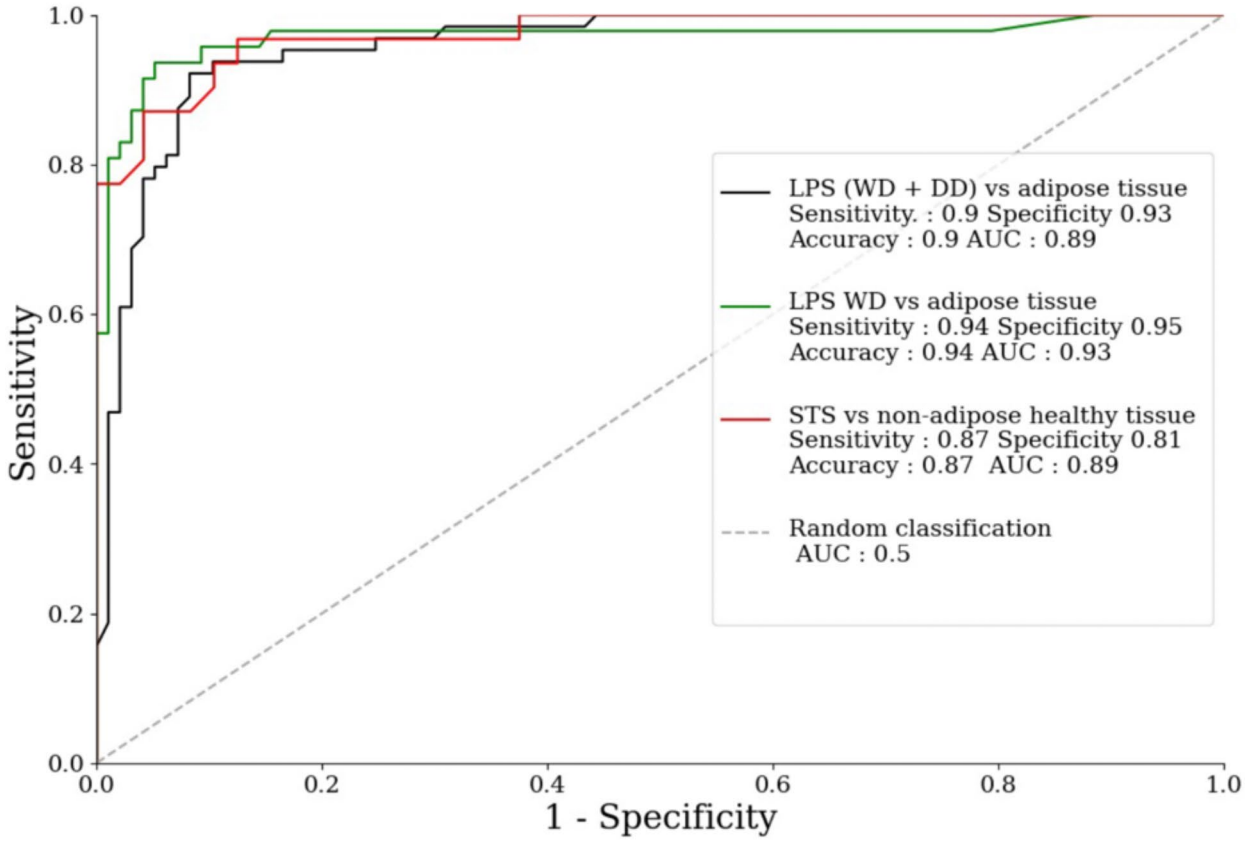


Fig. 5. ROC curves of three random forest classifying models: LPS (WD + DD) vs. healthy adipose tissue (black), WDLPS vs. healthy adipose tissue (green), and other STS vs. non-adipose, protein-rich healthy adipose tissue (red).

than 90% for liposarcomas, maintaining its performance in identifying well-differentiated liposarcomas. There are no accepted performance benchmarks against which to compare our results. However, there are no methods currently used on a regular basis for intraoperative tissue analysis during STS resection. Frozen section analysis, the mainstay of intraoperative tissue analysis, can rarely produce a diagnostic answer when used on STS samples given the difficulty and high level of expertise needed for STS pathological evaluation. Thus, an agreement greater than 90% with an expert pathologist is deemed satisfactory. The UltraProbe system has also shown that it uses integration times short enough to acquire tissue spectra almost in real time during surgical resection of STS without disrupting surgical workflow.

The high prediction accuracy obtained in classifying WDLPS Raman spectra is a strong indicator of the robustness of the technique used, and of the recent improvements in device performance. WDLPS is difficult to distinguish from healthy retroperitoneal fat during surgery through visual and tactile assessments. It is also difficult to establish a clear histopathological diagnosis of WDLPS, and expert sarcoma pathologists are required. A previous publication by Nguyen and al[55] studying Raman spectroscopy use in STS obtained high classification accuracy for most types of studied sarcomas but obtained negative results for WDLPS classification. Obtaining a classification accuracy of 94% indicates the UltraProbe's ability to obtain strong Raman signal and allows a classification that closely matches standard histopathological diagnosis.

STS present multiple clinical challenges due to their rarity and heterogenicity as a pathological entity. These same limitations also apply to our study. A limited number of patients with multiple distinct pathological entities has generated a rather small and unbalanced dataset. As a result, our classification has a higher risk of overfitting. However, small cohorts of patients are a problem present in most of the sarcoma literature, and its effects are also felt when applying machine learning algorithms to these datasets. Applying machine learning algorithms to smaller datasets often result in artificially high classification performance that often do not hold up as well in larger populational applications. However, the risk of overfitting is mitigated by our choices of validation methods, as well as by using random forests classifiers. This type of machine learning algorithm performs well with smaller datasets and is relatively resistant to overfitting.

These results demonstrate Raman spectroscopy's potential to be used as a technique for non-destructive, real-time tissue analysis during STS surgery. Its usefulness comes in part from its ability to provide tissue analysis quickly enough not to disrupt the flow of surgery. Given its ability to detect STS, it could potentially be used as an adjunct during STS surgery to decrease the rate of positive resection margins and improve patient outcomes.

The demonstrated acquisition times were fast enough that with a smaller number of Raman spectra used for new acquisitions, sub-second acquisitions are possible.

However, the probe's design as a point-probe interrogation device limits the surface area of the total resection margin that can be evaluated with a single measurement. As STS can be quite large tumors, point probe analysis cannot provide information on the entire resection margin. Wide field Raman spectroscopy could provide a solution to this problem, and recent work has been done towards developing this technique[56]. Current integration times in the range of five minutes per cm^2, currently limit its real-world applicability. Further, in clinical scenarios, the resection margin does not need to be examined in its entirety. Raman spectroscopy tissue analysis can often be targeted to areas that present a surgical challenge due to tumor location or anatomical proximity to vital structures. Despite the size of the area examined, the current point-probe system's speed and ease of use provide a net benefit as an adjunct tool to evaluate resection margin status intraoperatively.

The presented results are based on controlled measurements made on pre-selected sites that macroscopically appeared to contain a single type of tissue. The specific case of resection margins has not been directly studied, and Raman spectroscopy's ability to detect STS specifically at the margins of resection need to be inferred from its performance within the frame of our study. A direct assessment of its ability to detect positive resection margins requires follow up studies, with a larger patient population. Given the combined rarity of the disease and relative rarity of positive resection margins, sufficient statistical power could realistically only be achieved through large multi-center trials. To reduce class heterogeneity and increase the performance of the classification algorithms, subsequent studies could focus on STS subtypes that would benefit the most from intraoperative resection margin assessment, such as LPS and WDLPS more specifically. Such studies would give the opportunity to evaluate the impact of the use of Raman spectroscopy on positive margin resection rates, as well as the impact on patient outcome and survival following its use during sarcoma surgery. The impact of radiotherapy on Raman signal should also be evaluated in future studies. The presented results included only five patients that received neoadjuvant radiotherapy, with three different histological subtypes. The sarcoma samples analyzed from these patients were confirmed to contain viable residual sarcoma tissue, but the small size and heterogeneity of this patient subset prevented any meaningful analysis of the impact of radiotherapy on Raman signal for tissue within the same histologic diagnostic class.

Methods

Patient inclusion criteria

Participants were recruited from the patient population at Maisonneuve-Rosemont Hospital in Montreal, Canada. Adult patients referred to the surgical oncology and orthopedic oncology services for STS resection were considered. STS have a wide variety of histological subtypes. Included STS subtypes were limited to the most frequent subtypes encountered to avoid creating a dataset that included multiple single patients with a specific disease subtype. Included STS subtypes were liposarcomas, leiomyosarcomas, myxofibrosarcomas, solitary fibrous tumors, and undifferentiated pleomorphic sarcomas. Other subtypes of STS were excluded. Patients with a past medical history of connective tissue disorders were also excluded because of their potential impact on tissue signaling.

Raman spectroscopy instrumentation

Spectroscopic measurements were made using two different hand-held probe systems allowing single-point tissue interrogation at sub-millimeter scale (Fig. 1). Class 1 systems were associated with the optical design of all probe systems that were used by our group in the past to interrogate human tissue. For the new class of systems (Class 2: UltraProbe), optical design changes were made to the spectrometer and to the hand-held probe to optimize light collection efficiency.

The Raman spectroscopy systems consisted of a hand-held probe (EmVision LLC, FL, USA), a 350 milliwatts spectrally stabilized laser emitting in the near-infrared (NIR) at 785 nm (Innovative Photonic Solutions, NJ, USA), a high speed and high-resolution charge-coupled device (CCD) spectrometer (ANDOR Technology, Belfast, UK), and a computer controlling the optical hardware for data acquisition and processing. The data acquisition software allowed either of two modes of operation. In one mode (*manual*), each acquisition was performed at a pre-set laser power level at the probe tip (I) with accumulation time (T) per measurement that were repeated (at the same location) N times to optimize SNR. In a second mode of operation (*automated exposure control*), the laser power at the tip was pre-set but the accumulation T per measurement was automatically adjusted to maximize usage of the dynamical range of the CCD sensor for each of the N repeat measurements[52]. All tissue phantom experiments were performed using the *manual* mode, while all in-human tissue measurements (*in vivo* and *ex vivo*) were performed with the automatic exposure control activated.

The hand-held probe for the Class 1 instrument used seven 300 micrometer core collection multi-mode fibers (Fig. 1b). A donut-shaped long-pass filter that rejected the laser light and passed the Raman light from the sample was positioned in front of the collection fibers. These seven fibers surrounded a stainless-steel tube inside which the laser delivery fiber was inserted. The laser delivery fiber had a 300 micrometers core fiber. A band-pass filter was positioned in front of the excitation fiber to remove the Raman signal induced in the fiber. The two-piece converging front lens was made of a plano-convex 2 mm diameter curvature sapphire back portion, with a flat front portion of 1 mm thickness made of magnesium fluoride. This configuration was used to minimize the inelastic scattering contributions from the sapphire.

The new probe design (Class 2) incorporated a hole in the converging lens to allow laser excitation fibers to pass through the lens (Fig. 1b). This eliminated laser reflection off the surfaces of the converging lens. This had the effect of reducing scattered laser light within the probe itself, while minimizing potential interference from scattered laser light interacting with probe materials. A donut shaped lens filter was added to the Class 2 probe to block any backscattered laser light from the probe's distal tip or from the interrogated medium. This

reduced additional scattered laser light within the probe itself. A stepped window was also added to the Class 2 probe to reduce the window diameter, minimizing any light originating from sources other than the interrogated medium. Because of the additional number of fibers in the Class 2 probe, its tip outer diameter increased from 2.1 mm to 2.4 mm when compared to Class 1 probes.

The Class 1 spectrometer used seven 300 micrometers core fibers for light detection that were housed in a spring-loaded snap within a connector having a 100 μm slit with a height of 3.25 mm. The Class 2 spectrometer used twenty-one 300 micrometers core fibers housed in a similar connector, albeit with a slit with a height of 7.6 mm. To accommodate the increased number of input fibers, the Class 2 spectrometer utilized a larger, custom designed and manufactured front lens. This lens reduced the 250 micrometers slit width size of the Class 2 spectrometer to approximately that of the Class 1 spectrometer slit image size at the CCD. The 250 micrometers actual slit width used in the Class 2 spectrometer more than doubled the light input to the spectrometer compared to the Class 1 spectrometer, while the spectral resolution was equivalent to the Class 1 spectrometer. To accommodate the larger lenses and optics, the Class 2 spectrometer has a larger enclosure footprint.

In vivo and *ex vivo* spectroscopy data acquisition

After sterilization, the Class 2 hand-held Raman spectroscopy probe was taken to the operating room during STS resection surgery. In vivo spectra were acquired after closing all ceiling and surgical lights in the operating room, and care was taken to remove excess blood pooling in the surgical field. For every *in vivo* spectrum acquired, a tissue sample measuring approximately 10 mm was excised at the exact site where spectroscopy data was acquired. The site of tissue sampling was selected by the surgeon. Spectra were first acquired on healthy adipose, muscle, and fibrous (aponeurosis) tissues, at a location distant from the tumor. Then, following *en bloc* tumor resection, spectra were acquired on the same types of tissue in the tumor bed. The specimen was then brought to the pathology laboratory, where it was examined by a pathologist following margin inking and slicing. Following these steps, spectroscopic measurements were acquired on the central parts of the sliced sarcoma specimens to avoid ink contamination of the signal acquired while also avoiding compromising the pathological evaluation of the resection margins. Given the open working environment of the pathology laboratory, only the lights directly above the working bench were turned off, while the ceiling lights were left open during the measurements taken *ex vivo*.

Spectral pre-processing

Standard signal processing steps were applied to all individually acquired spectra to isolate the contribution associated with inelastic scattering, i.e. Raman scattered photons[57]. The acquisitions obtained for a single point were averaged, and background signal was removed. Cosmic rays were removed using an in-house algorithm based on finding narrow peaks of high intensity[53]. The *x*-axis was then calibrated using an acetaminophen tab, and the *y*-axis calibration was done using a standard reference material (NIST SRM-2241 for 785 nm excitation). A Savitzky-Golay filter of order 3 with a window of 11 was applied for signal smoothing. Baseline signal removal was done using the BubbleFill algorithm[53]. Standard normal variate (SNV) normalization of the spectra was done for every spectrum. Spectrum quality was assessed using the average signed squared intensity (ASSI) quality factor (QF)[53]. This metric assigned a value between 0 and 1 to a SNV normalized signal, favoring narrow high-intensity peaks, and penalizing wide, low-intensity peaks. Pure noise would receive a score close to 0 while measurements associated with high quality Raman spectra have a quality factor closer to 1. Using the ASSI metric, every spectrum with a QF inferior to 0.6 was discarded, allowing only higher quality spectra to be used in the machine learning models datasets. Ambient light contamination was seen in multiple spectra in bands located at 950–1050, 1310–1370 cm^{-1} and 1500–1650 cm^{-1}. Bands located at 1310–1370 cm^{-1} and 1500–1650 cm^{-1} do not correspond to known relevant biological compounds, and to ensure that no bias was introduced in the classification model, the signal in these regions was smoothed out. This was done by selectively decreasing the size of the bubble used in the BubbleFill algorithm only in these regions. The majority of the spectra obtained *ex vivo* in the pathology laboratory contained significant light contamination in the band located at 950–1050 cm^{-1}. This region also contains a characteristic phenylalanine peak associated with protein-rich tissues. However, since light contamination in this band occurred exclusively in *ex vivo* spectra, it would have induced a significant bias in the classification model. To avoid this, the region was also smoothed out using the BubbleFill algorithm.

Data consistency between ex vivo and in vivo datasets

Out of the 30 patients recruited as part of the study, five were selected to further evaluate potential time-dependent changes in Raman scattering signal following tissue excision. For each patient, five healthy tissue samples were selected : 2 healthy adipose tissue samples, 2 muscle tissue samples, and 1 fibrotic (aponeurosis) tissue sample. The selected specimens appeared macroscopically homogenous. An in vivo measurement was first obtained for each sample. An area approximately 10–15 mm surrounding a central point where the measurement was taken was then resected.

The resected specimen was then placed on a table covered by sterile surgical drapes. Spectroscopic measurements were then made at 1, 5, 10, 15, 30, 45, 60 and 90 min following specimen resection. Some Raman spectra acquired were contaminated by signal from the underlying sterile drape. To remove the contaminating signal from the tissue signal, reference spectra were taken from the sterile drape itself and averaged. A systematically present peak seen at 1500 cm^{-1} , not seen in biological tissues, was used as a reference peak for intensity calibration. For every sample spectrum, the average drape spectrum was scaled using the aforementioned reference peak, and the scaled average spectrum was subtracted from the sample spectrum to remove drape contamination. A two-sample Kolmogorov-Smirnov test was then used, and the corrected spectrum rejected if the test's p-value was superior to 0.0001. For every tissue type, the spectra for every time point were averaged for

comparison. Representative results obtained from the adipose tissue samples are summarized in Supplementary Fig. 1. For every tissue type, the Raman spectra from the different timepoints were averaged. The average spectra for every time point were then compared to ensure no time-dependent intensity modulation was present. The six highest peaks for all spectra were identified, and their intensity values compared at the different time points. No significant systematic differences were found between Raman spectra obtained *in vivo* for adipose, muscle, and fibrotic tissue samples.

Cancer detection machine learning model

A Raman spectra dataset was created following spectral acquisitions as detailed previously. For each Raman spectrum, the exact location of the acquisition was excised and examined by an expert pathologist to provide a histopathologic diagnosis to be used as a label for the spectrum. This histology-based label ensured that although different tissue types were present in the specimen, every Raman spectrum in the dataset was labelled according to the tissue type that was used to obtain the signal. Any variations in tissue type and tumor grade within the examined specimen were thus recognized as such and were associated with the appropriate label. The dataset was subdivided into distinct datasets that were used to train the different machine learning classifiers used for distinct clinical situations. A first dataset included spectra from healthy adipose tissue and adipose rich sarcomas: WDLPS and DDLPS. Macroscopic differentiation between liposarcomas and non-adipose healthy tissue does not represent a challenge to surgeons, and Raman based identification for this scenario is of little value. Differentiating between healthy adipose tissue and liposarcomas is very challenging, and a classifier for this purpose answers a strong clinical need. As WDLPS is both the most frequent RSTS subtype and the most difficult subtype to distinguish from healthy adipose tissue, a classifier was built specifically for detecting WDLPS from healthy adipose tissue. Another subset was created, including Raman spectra from all protein-rich tissue samples (non-adipose tissue). The healthy tissue included were muscle, fibrosis, and necrosis. The STS included were LMS, SFT, UPS, and MFS. This subset was used to create a classifier that could identify non-liposarcoma STS from non-adipose, protein-rich healthy tissue.

Following spectral pre-processing, feature selection was done using a random forest classifier with 100 estimators to classify using only the features that corresponded to significant information and contributed the most to class discrimination. The feature scores were visualized to ensure that the selected features corresponded to peaks seen on the Raman spectra. The number of selected features corresponded to a hyperparameter that was be optimized for the final classifier. After feature selection, three classifiers were produced using a random forest algorithm. The WDLPS vs. healthy adipose tissue classifier used 200 estimators and 125 features. The WDLPS + DDLPS vs. healthy adipose tissue classifier used 200 estimators and 200 features. The STS vs. non-adipose tissue classifier used 200 estimators and 200 features. The number of estimators and the number of selected features were optimized using a grid search function. The number of estimators was tested for values ranging from 10 to 250, and the number of selected features was tested for values ranging from 20 to 250. Classes were asymmetrically weighted in favor of sarcoma classes, given the uneven distribution of spectra between healthy and sarcoma labels in the dataset. Five-fold cross-validation was used to compare prediction performance with histopathology labels. A receiver operating characteristics (ROC) curve was generated to determine the parameters producing the best performance.

Data availability

The main data supporting the findings of this study are available within the Article and its Supplementary Information. The raw data generated during the study is too large to be publicly shared, yet it is available for research purposes from the corresponding author upon reasonable request.

Code availability

Source code used in this work is available for non-commercial purposes from the corresponding author on request.

Received: 2 August 2024; Accepted: 4 March 2025
Published online: 14 March 2025

References

1. WHO Classification of Tumours Soft Tissue and Bone Tumours (IARC Press, 2020).
2. Porter, G. A., Baxter, N. N. & Pisters, P. W. Retroperitoneal sarcoma: a population-based analysis of epidemiology, surgery, and radiotherapy. *Cancer* **106**(7), 1610–1616 (2006).
3. Al, M. T. A. Retroperitoneal sarcomas: patterns of care at diagnosis, prognostic factors and focus on main histological subtypes: a multicenter analysis of the French sarcoma group. *Ann. Oncol.* **25** (3), 735–742 (2014).
4. Bagaria, S. P. and al, The volume-outcome relationship in retroperitoneal soft tissue sarcoma: Evidence of improved short- and long-term outcomes at high-volume institutions, *Sarcoma* **2018**, 3056562 (2018).
5. Dingley, B., Fiore, M. & Gronchi, A. Personalizing surgical margins in retroperitoneal sarcomas: an update, (in eng). *Expert Rev. Anticancer Ther.* **19** (7), 613–631 (2019).
6. Anaya, D. A., Lev, D. C. & Pollock, R. E. The role of surgical margin status in retroperitoneal sarcoma. *J. Surg. Oncol.* **98** (8), 607–610 (2008).
7. Kirane, A. & Crago, A. M. The importance of surgical margins in retroperitoneal sarcoma. *J. Surg. Oncol.* **113**(3), 270–276 (2016).
8. Singer, S., Antonescu, C. R., Riedel, E. & Brennan, M. F. Histologic subtype and margin of resection predict pattern of recurrence and survival for retroperitoneal liposarcoma. *Ann. Surg.* **238** (3), 358–370 (2003).
9. Abdelfatah, E. and al., a., Long-term outcomes in treatment of retroperitoneal sarcomas: A 15 year single-institution evaluation of prognostic features. *J. Surg. Oncol.* **114**(1), 56–64 (2016).
10. Khan, S. and al., a., Is microscopic margin status important in retroperitoneal sarcoma (RPS) resection? A systematic review and metaanalysis, *Can. J. Surg.* **65** (2022).

11. Bonvalot, S. Primary retroperitoneal sarcomas: a multivariate analysis of surgical factors associated with local control. *J. Clin. Oncol.* **27** (7), 31–37 (2009).
12. Stahl, J. M. and al., a., The effect of microscopic margin status on survival in adult retroperitoneal soft tissue sarcomas. *Eur. J. Surg. Oncol. (EJSO)* **43**(1), 168–174 (2017).
13. Paik, B. A systematic review of margin status in retroperitoneal liposarcomas: does the R0 margin matter? *Front. Oncol.* **12**, 891710 (2022).
14. Guo, Q., Zhao, J., Du, X. & Huang, B. Survival outcomes of surgery for retroperitoneal sarcomas: A systematic review and meta-analysis. *PLoS One* **17** (7), e0272044 (2022).
15. Gronchi, A. & al Frontline extended surgery is associated with improved survival in retroperitoneal low- to intermediate-grade soft tissue sarcomas. *Ann. Oncol.* **23** (4), 1067–1073 (2012).
16. Bonvalot, S. and al., a., Aggressive surgery in retroperitoneal soft tissue sarcoma carried out at high-volume centers is safe and is associated with improved local control, *Ann Surg Oncol* **17**(6), 1507–1514 (2010).
17. Bonvalot, S. & al Preoperative radiotherapy plus surgery versus surgery alone for patients with primary retroperitoneal sarcoma (EORTC-62092: STRASS): a multicentre, open-label, randomised, phase 3 trial. *Lancet Oncol.* **21** (10), 1366–1377 (2020).
18. Miura, J. T. Impact of chemotherapy on survival in surgically resected retroperitoneal sarcoma. *Eur. J. Surg. Oncol. (EJSO)*. **41** (10), 1386–1392 (2015).
19. Italiano, A. & al Effect of adjuvant chemotherapy on survival in FNCLCC grade 3 soft tissue sarcomas: a multivariate analysis of the French sarcoma group database. *Ann. Oncol.* **21** (12), 2436–2441 (2010).
20. Almond, L. M., Strauss, A. G. D., Jafri, M., Ford, S. & Desai, A. Neoadjuvant and adjuvant strategies in retroperitoneal sarcoma. *Eur. J. Surg. Oncol.* **44** (5), 571–579 (2018).
21. Sanctis, R. D. Long-term follow-up and post-relapse outcome of patients with localized retroperitoneal sarcoma treated in the Italian sarcoma group-soft tissue sarcoma (ISG-STS) protocol 0303. *Ann. Surg. Oncol.* **24** (13), 3872–3879 (2017).
22. Sanfilippo, R. High-dose continuous-infusion Ifosfamide in advanced well-differentiated/dedifferentiated liposarcoma. *Clin. Sarcoma Res.* **4** (1), 16 (2014).
23. Gronchi, A. (ed) al., a., Neoadjuvant chemotherapy in high-risk soft tissue sarcomas: final results of a randomized trial from Italian (ISG), Spanish (GEIS), French (FSG), and Polish (PSG) Sarcoma groups, *Journal of Clinical Oncology*, vol. 38`, no. 19, pp. 2178–2186, (2020).
24. Graves, P. & Gardiner, D. Practical Raman spectroscopy, *Springer-Verlag* **10**, 978–983 (1989).
25. Orlando, A. and al, a., A comprehensive review on Raman spectroscopy applications, *Chemosensors* **9**(9) (2021).
26. Butler, H. J. and al., a., Using Raman spectroscopy to characterize biological materials. *Nat. Protoc.* **11**(4), 664–687 (2016).
27. Smith, E. & Dent, G. *Modern Raman Spectroscopy: a Practical Approach* (Wiley, 2019).
28. Choo-Smith, L. P. and al, a., Medical applications of Raman spectroscopy: from proof of principle to clinical implementation, *Biopolymers* **67**(1), 1–9 (2002).
29. Movasaghi, Z. & Rehman, I. U. S. R. and Raman spectroscopy of biological tissues. *Appl. Spectrosc. Rev.* **42**(5), 493–541 (2007).
30. Czamara, K. et al. Raman spectroscopy of lipids: a review. **46**(1), 4–20 (2015).
31. Hanlon, E. B. Prospects for in vivo Raman spectroscopy. *Phys. Med. Biol.* **25**(2), R1 (2000).
32. Krause, B. R. & Hartman, A. D. Adipose tissue and cholesterol metabolism. *J. Lipid Res.* **25** (2), 97–110 (1984). 1984/02/01/.
33. Chan, J. W. et al. Micro-Raman spectroscopy detects individual neoplastic and normal hematopoietic cells. *Biophys. J.* **90**(2), 648–656 (2006).
34. [34] Cheng, M., Bhujwalla, Z. M. & Glunde, K. Targeting phospholipid metabolism in cancer. *Front. Oncol.* **6**, 266 (2016).
35. Hanna, K. et al. Raman spectroscopy: current applications in breast cancer diagnosis, challenges and future prospects. *Br. J. Cancer* **126** (8), 1125–1139 (2022).
36. Zúñiga, W. C. et al. Raman spectroscopy for rapid evaluation of surgical margins during breast cancer lumpectomy. **9**(1), 14639 (2019).
37. Zhang, L. et al. Raman spectroscopy and machine learning for the classification of breast cancers. **264**, 120300 (2022).
38. Zhou, Y. et al. Optical biopsy identification and grading of gliomas using label-free visible resonance Raman spectroscopy. *J. Biomed. Opt.* **24** (9), 1–12 (2019).
39. Livermore, L. J. et al. Rapid intraoperative molecular genetic classification of gliomas using Raman spectroscopy, *Neurooncol. Adv.* **1**(1), vdz008 (2019).
40. Hollon, T. & Orringer, D. A. Label-free brain tumor imaging using Raman-based methods. *J. Neurooncol.* **151** (3), 393–402 (2021).
41. Liu, K., Zhao, Q., Li, B. & Zhao, X. Raman spectroscopy: a novel technology for gastric cancer diagnosis. *Front. Bioeng. Biotechnol.* **10**, 856591 (2022).
42. Noothalapati, H., Iwasaki, K. & Yamamoto, T. Non-invasive diagnosis of colorectal cancer by Raman spectroscopy: Recent developments in liquid biopsy and endoscopy approaches. *Spectrochim. Acta A Mol. Biomol. Spectrosc.* **258**, 119818 (2021).
43. I, P. S. et al. Improving clinical diagnosis of early-stage cutaneous melanoma based on Raman spectroscopy. *Br. J. Cancer* **119** (11), 1339–1346 (2018).
44. Ember, K. et al. In situ brain tumor detection using the Raman spectroscopy sentry system—Results of a multicenter study. *Sci. Rep.*
45. Jermyn, M. et al. Intraoperative brain cancer detection with Raman spectroscopy in humans. *Sci. Transl. Med.* **7**, 274 (2015).
46. Desroches, J. et al. Characterization of a Raman spectroscopy probe system for intraoperative brain tissue classification. *Biomed. Opt. Express* **6** (7), 2380–2397 (2015).
47. David, S. et al. In situ Raman spectroscopy and machine learning unveil biomolecular alterations in breast cancer. *J. Biomed. Opt.* **28** (3), 360009 (2023).
48. Picot, F. et al. Image-guided Raman spectroscopy navigation system to improve transperineal prostate cancer detection. Part 1: overview of Raman spectroscopy fiber-optics system and in-situ tissue characterization. *J. Biomed. Opt.* **27** (9), 95003 (2022).
49. Aubertin, K. et al. March., Mesoscopic characterization of prostate cancer using Raman spectroscopy: potential for precision diagnostics and therapeutics. *Br. J. Urol. Int.* (2018).
50. Leblond, F. et al. Sub-second lung cancer detection within an heterogenous background of normal and benign tissue using single-point Raman spectroscopy. *J. Biomed. Opt.* **28** (9), 90501 (2023).
51. David, S. et al. Multispectral label-free Raman spectroscopy can detect ovarian cancer within the abdominopelvic cavity with high accuracy. *J. Biophotonic* (2021).
52. Dallaire, F. et al. Method for quantitative spectral quality assessment applied to Raman spectroscopy measurements in surgical applications. *J. Biomed. Opt.* **25** (4), 040502 (2020).
53. Sheehy, G. et al. Open-sourced Raman spectroscopy data processing package implementing a novel baseline removal algorithm validated from multiple datasets acquired in human tissue and biofluids. *J. Biomed. Opt.* **28** (2), 025002 (2023).
54. Kerr, L. T., Byrneb, H. J. & Hennellyac, B. M. Optimal choice of sample substrate and laser. *Anal. Methods*. **7**, 5041–5052 (2015).
55. Nguyen, J. Q. et al. Intraoperative Raman spectroscopy of soft tissue sarcomas. *Lasers Surg. Med.* **48**(8), 774–781 (2016).
56. Daoust, F. et al. A clinical Raman spectroscopy imaging system and safety requirements for in situ intraoperative tissue characterization, *Analyst*. https://doi.org/10.1039/D2AN01946A **148**(9), 1991–2001 (2023).
57. Ember, K. et al. Detection of COVID-19-infected saliva in a real-world setting using label-free Raman spectroscopy and machine learning. *J. Biomed. Opt.* **27** (2), 0250022 (2021).

Author contributions

JPD : Conceptualization, methodology, investigation, formal analysis, validation, data curation, visualization (Figs. 4 and 5-S1), writing – original draft, writing – review & editing. ALM: Methodology, data curation, formal analysis, visualization (Figs. 1 and 2-3), writing- original draft, writing – review & editing. FD: Methodology, software, formal analysis, writing – review and editing. JD : Conceptualization, methodology, data curation. KU : Methodology, resources. EM : Methodology, resources. GL : Data curation. GB : Data curation. SM : Data curation. MI : Data curation. FL : Conceptualization, investigation, methodology, supervision, project administration, writing – original draft, writing – review & editing. MKG: Conceptualization, investigation, methodology, supervision, project administration, writing – original draft, writing – review & editing.

Declarations

Competing interests

Frédéric Leblond co-founded Reveal Surgical, a medical device company that seeks to commercialize a Raman spectroscopy system for intraoperative cancer detection.The other authors have no competing interests to declare.

Human participants consent and ethics

Informed and written consent was obtained from all participants. The study was approved by the Ethics Committee of the Maisonneuve-Rosemont Hospital, which follows guidelines from the Tri-council policy statement Ethical Conduct for Research Involving Humans – TCPS 2, and the United States Code of Federal Regulations overseeing human research.

Additional information

Supplementary Information The online version contains supplementary material available at https://doi.org/10.1038/s41598-025-93089-z.

Correspondence and requests for materials should be addressed to F.L. or M.-K.G.

Reprints and permissions information is available at www.nature.com/reprints.

Publisher's note Springer Nature remains neutral with regard to jurisdictional claims in published maps and institutional affiliations.

Open Access This article is licensed under a Creative Commons Attribution-NonCommercial-NoDerivatives 4.0 International License, which permits any non-commercial use, sharing, distribution and reproduction in any medium or format, as long as you give appropriate credit to the original author(s) and the source, provide a link to the Creative Commons licence, and indicate if you modified the licensed material. You do not have permission under this licence to share adapted material derived from this article or parts of it. The images or other third party material in this article are included in the article's Creative Commons licence, unless indicated otherwise in a credit line to the material. If material is not included in the article's Creative Commons licence and your intended use is not permitted by statutory regulation or exceeds the permitted use, you will need to obtain permission directly from the copyright holder. To view a copy of this licence, visit http://creativecommons.org/licenses/by-nc-nd/4.0/.

© The Author(s) 2025